Size effects in microstructured superconductors and quantum materials

Fermin, R.

Mesoscopic S−F-hybrid Josephson junctions

2
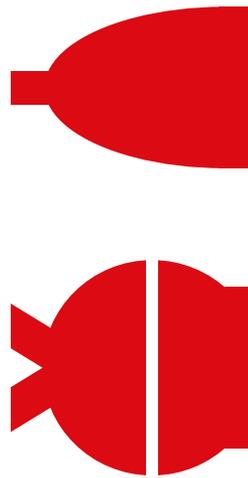
4

SUPERCONDUCTING TRIPLET RIM CURRENTS IN A SPIN-TEXTURED FERROMAGNETIC DISK

R. Fermin, D. van Dinter, M. Hubert, B. Woltjes, M. Silaev, J. Aarts & K. Lahabi

Since the discovery of the long-range superconducting proximity effect, the interaction between spin-triplet Cooper pairs and magnetic structures such as domain walls and vortices has been the subject of intense theoretical discussions, while the relevant experiments remain scarce. Using the procedure from Chapter 3, we fabricate disk-shaped Josephson junctions with a ferromagnetic cobalt barrier, which features a highly controllable spin texture. Here, the vortex magnetization of Co and the Cooper pairs of Nb conspire to induce long-range triplet (LRT) superconductivity in the ferromagnet. Surprisingly, the LRT correlations emerge in highly localized (sub-80 nm) channels at the rim of the ferromagnet, despite its trivial band structure. We show that these robust rim currents arise from the magnetization texture acting as an effective spin-orbit coupling, which results in spin accumulation at the bilayer–vacuum boundary. Lastly, we demonstrate that both 0 and π channels can be realized in the same device by altering the spin texture of the ferromagnet.

4.1. INTRODUCTION

The appearance of localized supercurrents at the edges of a Josephson junction is generally attributed to the topology of the electronic band structure and edge states[1]. Edge states and the accompanying edge currents are typically found in ultraclean systems such as 2D electron gases[2], nanowires[3], and graphene[4]. Here, we report the emergence of highly localized (sub-80 nm) spin-polarized supercurrents at the rim of disk-shaped Josephson junctions with a diffusive ferromagnetic barrier (Co). As we demonstrate, however, the rim currents are not related to the electronic band structure but rather a direct result of the interactions between spin-triplet Cooper pairs and the non-trivial spin texture of the ferromagnet.

At the interface between a superconductor and a ferromagnet, short-range triplet (SRT; in Dirac notation $\frac{1}{\sqrt{2}}(|\uparrow\downarrow\rangle + |\downarrow\uparrow\rangle)$, i.e., triplets without spin projection along the quantization axis) Cooper pairs with zero spin projection emerge naturally via spin-mixing of singlet pairs and decay over a few nanometers ($\xi_F(Co) \sim 3$ nm [5]) inside the ferromagnet. Long-range triplet (LRT, in Dirac notation $|\uparrow\uparrow\rangle$ and $|\downarrow\downarrow\rangle$) pairs can, on the other hand, propagate over substantially larger distances[6, 7]. Half-metallic systems can even show the LRT proximity effect over hundreds of nanometers[8–11]. Due to their spin polarization, the LRT Cooper pairs can provide the means to combine the absence of Joule heating and decoherence with the functionality of spintronic devices[12, 13]. However, the controlled generation of LRT currents has proven to be a demanding process, commonly realized in complex superconductor-ferromagnet hybrids, involving multiple F layers with noncollinear magnetization[14–24]. Furthermore, a substantial body of research considered the possibility of generating and controlling LRT correlations using spin-textured systems, such as domain walls[6, 25–28] and vortices[29, 30]. However, the experimental evidence to verify such models remains scarce[31]. In other recent developments, it was suggested that theoretically, spin mixing can also be achieved by spin-orbit coupling (SOC)[32–36]. This led to researching long-range proximity effects with Josephson junctions containing heavy metal interlayers[37–43]. In addition, recent studies suggest that spin-orbit coupling (SOC) can lead to spin accumulation at the edges of Josephson devices[35, 44, 45] and, in some cases, generation of LRT currents[46–49]. At present there is a complete lack of experiments that can examine the influence of SOC on LRT transport. As a consequence, the interplay between triplet pairing and magnetic texture as well as SOC remains elusive.

To address these issues, we use the control of the junction geometry gained in Chapter 3 to fabricate disk-shaped S−F−S Josephson junctions that feature a ferromagnetic vortex spin texture capable of converting singlet Cooper pairs into LRT currents. These exhibit a (~ 20 nm) cobalt weak link, which eliminates any singlet or SRT transport. We show that a magnetization gradient of the vortex can act as an effective SOC, which leads to spin accumulation at the rims of the device. This is verified by our transport experiments, which show that the LRT transport is highly localized at the rims of the
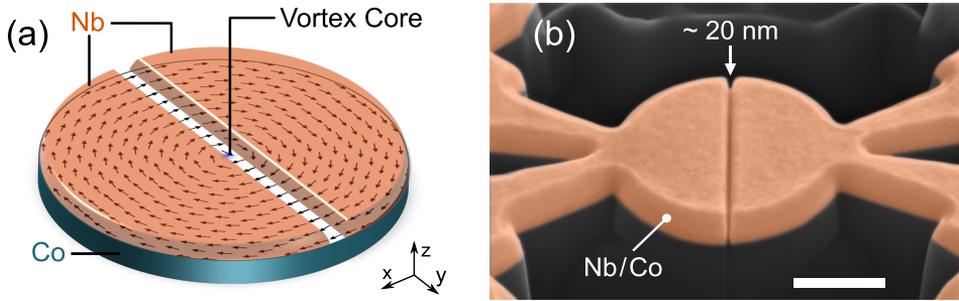
Figure 4.1: (a) Schematic of the Josephson device. The Nb electrodes are separated by a trench, forming a Co weak link. The pattern on the Co layer corresponds to micromagnetic simulations of a micrometer-size disk. (for more information on the micromagnetic simulations, see Appendix A of Chapter 5). The arrows correspond to the in-plane magnetization, while the out-of-plane component is represented by color, which only appears at the vortex core (blue region; less than 5 nm in diameter). Schematic courtesy of Kaveh Lahabi. (b) False colored scanning electron micrograph of a structured bilayer. The 20 nm gap indicates the Co weak link at the bottom of the trench. The scale bar is equivalent to 400 nm.

ferromagnet, resulting in a distinct double-slit supercurrent interference pattern. By modifying the spin texture in a controllable manner, we show that both 0 and π segments can emerge in a single junction. Utilizing the linearized Usadel equation, we examine the microscopic origin of the rim currents in the proximized ferromagnet. Our findings suggest that, in addition to spin texture, superconductor-vacuum boundary conditions play an essential role in the singlet to LRT conversion.

4.2. ESTABLISHING LONG-RANGE TRIPLET TRANSPORT

Using equal methods as introduced in Chapter 3, we fabricate S−F−S disk junctions from an Nb/Co bilayer (thickness of 45 nm and 60 nm, respectively). Generally, in a disk-shaped ferromagnet of these size ranges, the magnetic moments will align in a vortex magnetization pattern[50, 51]. Therefore, we obtain a weak link containing a ferromagnetic vortex coupled by two superconducting leads. A schematic representation of such a junction is shown in Figure 4.1a, along with a false colored scanning electron micrograph of an actual device in Figure 4.1b. Figure 4.2a shows resistance as a function of temperature for a typical disk junction. A micron-wide weak link has a resistance of 200 mΩ and becomes fully proximized at low temperatures. We unambiguously establish the Josephson transport in our device by observing their Shapiro response to microwave radiation. The IV-curves show clear Shapiro steps (discrete voltage steps of $hf/2e$, where h is the Planck constant, f is the frequency, and e is the electron charge), which is a result of the phase-locking between the applied microwaves and the Josephson currents (see Figure 4.2(b)).
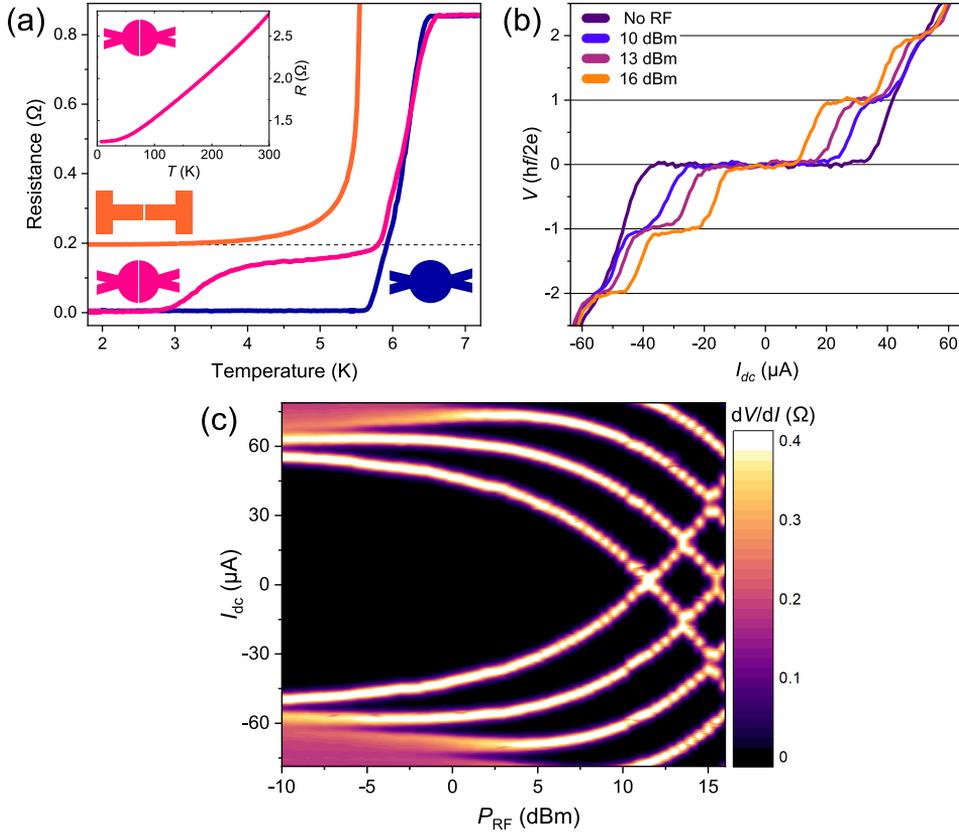
Figure 4.2: Overview of the basic transport properties of the devices. (a) Resistance as a function of temperature of a proximized disk device (pink) is compared to a Co−Nb disk without a trench (blue) and a bar-shaped device with uniform magnetization (orange). The bar-shaped device is not proximized due to the lack of spin texture (for more information, see Appendix A). (b) IV-characteristics at 2 K of a proximized disk device, measured while irradiating the sample with $f = 1.1$ GHz of microwave radiation for different powers. The voltage is normalized in units of $hf/2e$. (c) Evolution of the Shapiro response as a function of RF power represented as dV/d$I(\Omega)$ color map.

A direct method to examine the presence of LRT correlations is to verify that the proximity effect will disappear once the mechanism for the emergence of LRT pairing is eliminated. For instance, in the case of S/F′/F/F′/S multilayer junctions used in previous studies, where the generation of LRT correlations requires a magnetic non-collinearity between the F and F′ layers, the control experiment would show that I_c is heavily suppressed if the F′ layers were either removed or magnetized parallel (or antiparallel) to the F layer[15, 16, 18, 20, 23, 52]. The same argument applies here: if the proximity effect is due to LRT correlations produced by the spin texture of the junction, the I_c must vanish once the magnetization is uniform. We verify this through two experiments described in Appendix A. First, we examined the transport in bar-shaped control samples, where shape anisotropy ensures that (even in the absence of in-plane fields) the cobalt layer has a uniform magnetization along the long axis of the bar (see

Figure 4.2a and Figure A.1). These samples were fabricated via the same procedure as the primary disk-shaped junctions and received the same FIB treatment to structure their weak link. This is evident by the fact that the bar-shaped junctions and the disk devices have a matching barrier resistance ($\approx$ 200 mΩ). Despite multiple attempts, however, the bar-shaped control samples show no sign of long-range proximity. We also prepared disk-shaped control junctions where, by applying a lower dose of Ga-ions when structuring the weak link, we leave some residual Nb at the bottom of the trench, forming a nonmagnetic channel for singlet transport. Such junctions are completely insensitive to the magnetic state of the cobalt disk and are robust against the in-plane fields used for altering the spin texture; they maintain their I_c at fields as high as 2 T (see Figure A.3b). In contrast, for the triplet devices, this happens when we remove the spin texture by applying an in-plane field of 180 mT, which completely suppresses the I_c (see Figure A.3a).

4.3. TRIPLET CURRENTS CONFINED TO THE RIMS OF THE DISK

We establish the presence of rim currents by obtaining $I_c(B)$ of our junctions. Note that the out-of-plane fields used in these experiments are too small to disturb the stable vortex magnetization of the Co disk.

In a conventional S$-$N$-$S junction, the supercurrent is distributed uniformly across the weak link, yielding the interference patterns presented in Chapter 3. As shown in Figure 4.3, our S$-$F$-$S devices show a completely different behavior: two-channel interference patterns characterized by equal-width lobes and slow decay of oscillation amplitude. All the triplet junctions we measured (over ten devices) show such a two-channel interference pattern. This is illustrated in Figure 4.3, where we show the $I_c(B)$-patterns for two junctions with different diameters (1.62 and 1.05 µm). Note that the period of the oscillations scales inversely with the area of the junction, which is determined by the radius of the disk. We apply inverse Fourier transform to the $I_c(B)$-patterns to reconstruct the spatial distribution of supercurrent density. Figure 4.3 shows the results of our Fourier analysis for both devices. Regardless of the sample area, we consistently find the supercurrent to be highly localized at the rim of the sample: the rim current channels are 70 nm or less in width, limited by the resolution of the Fourier analysis[1]. Furthermore, the channels are highly symmetric, as indicated by the sharp cusps of the $I_c(B)$-pattern. Note that the trench is deepest on the sides of the disk (due to the geometry dependence on the milling rate, as can be seen by the small notches on the sides of the disk in Figure 4.1b), making the formation of accidental singlet edge channels even

---

[1]Here we have used the linear approximation of $f\left(\frac{y}{W}\right)$ to improve resolution, see section 3.4.1. In the published version of this chapter, we carried out the analysis by establishing a scaling relation between the period of the oscillations and the diameter of the disk. Here I adapted the Fourier analysis to incorporate the results from Chapter 3.
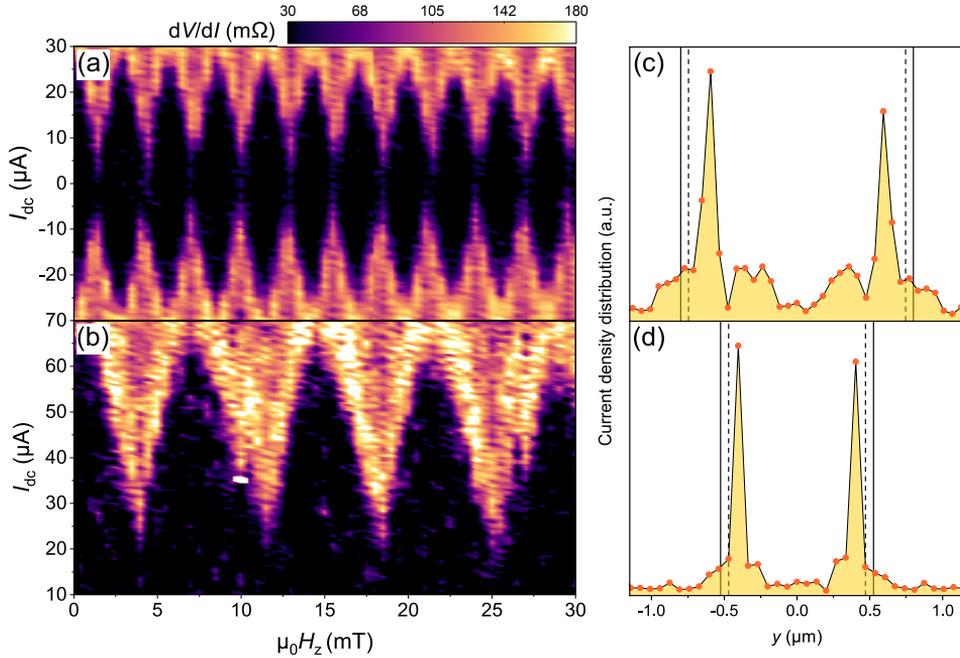
Figure 4.3: (a) and (b) Show superconducting interference patterns of two junctions with different diameters. The pattern is obtained by measuring the differential resistance as a function of d.c. current and magnetic field. The disk diameters in (a) and (b) are 1.62 μm and 1.05 μm, respectively. The period of the oscillations scales inversely with the junction area. In both cases, the junctions show a clear two-channel interference pattern. (c) and (d) depict the critical current density profiles obtained by the Fourier analysis of the patterns in (a) and (b) respectively. The vertical lines indicate the boundaries of the device.

less probable. More importantly, the two-channel behavior is completely absent in all the singlet control samples. If the barrier contains residual Nb, the junction yields a standard single-channel diffraction pattern (Figure A.2). Similarly, the current density in the S−N−S disk devices presented in Chapter 3 is distributed uniformly. This means the two-channel behavior is not a trivial result of the disk geometry.

4.4. ALTERING THE MAGNETIC TEXTURE BY AN IN-PLANE FIELD

So far, we have shown the unconventional distribution of supercurrents through the spin-textured ferromagnetic weak link. We investigate this further by modifying the spin texture using an in-plane magnetic field. Our micromagnetic simulations show that in-plane fields can alter the spin texture by effectively moving the vortex core along the axis perpendicular to the field (see Figure 4.4). For small in-plane fields, the core displacement has an almost linear response and is fully reversible. Using a vector magnet system, we can apply a constant in-plane magnetic field while simultaneously acquiring the $I_c(B)$-pattern as described above. Figure 4.4 shows the $I_c(B)$-patterns mea-
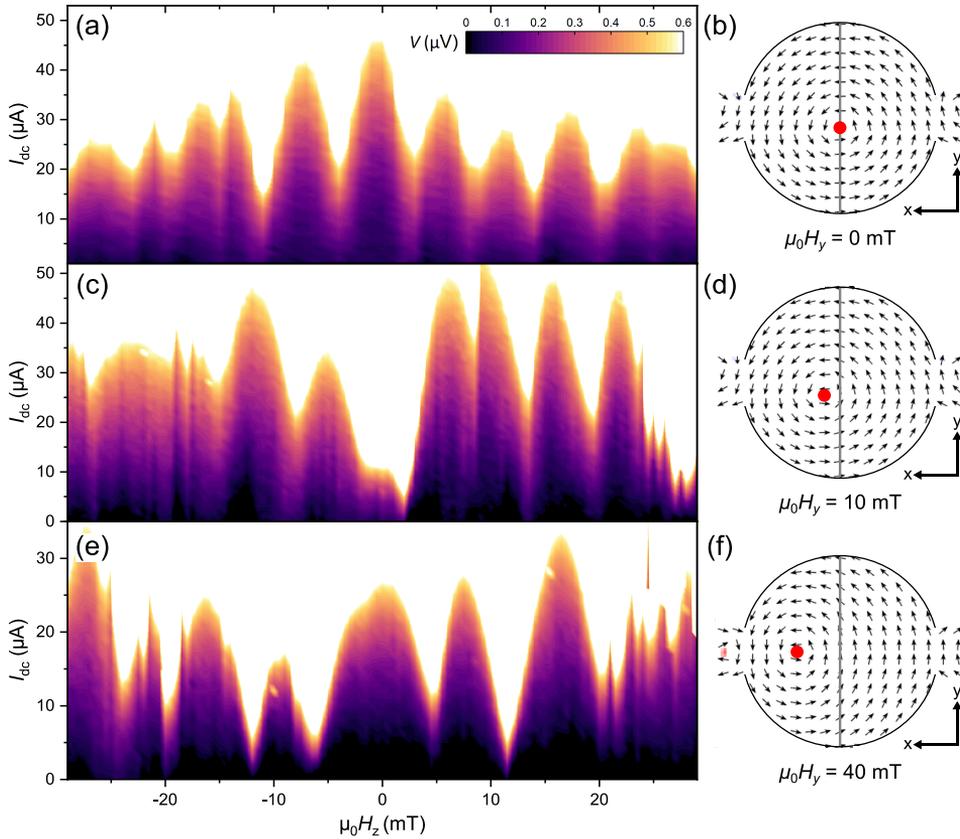
Figure 4.4: Supercurrent interference patterns (left column) measured at different in-plane fields and the corresponding simulated spin textures (right column). The gray line represents the position of the weak link, and the red dot indicates the location of the vortex core. (a) and (b) At zero in-plane field, the vortex is at the center of the disk, and a SQUID pattern is observed, i.e., lobes of equal width and slow decay of peak height. (c) and (d) Applying $\mu_0 H_y = 10$ mT breaks the axial symmetry of the vortex magnetization. This results in the suppression of the middle peak in the interference pattern, characteristic of a $0 - \pi$ SQUID. (e) and (f) At $\mu_0 H_y = 40$ mT the vortex core is displaced by over 100 nm. The middle peak of the interference pattern is recovered, and its width is doubled with respect to the original pattern. The peak height increases as a function of the out-of-plane field, regardless of sweep direction.

sured for different in-plane fields, applied along the trench (y-axis), together with the corresponding micromagnetic simulations.

At zero in-plane field (Figure 4.4a), we observe the aforementioned two-channel (SQUID) interference pattern, with maximum I_c at zero field. At $\mu_0 H_y = 10$ mT we observe a strong suppression of I_c for zero out of plane field. Remarkably, however, I_c is recovered upon increasing the out-of-plane field in either direction. The resulting $I_c(B)$-pattern bears a resemblance to a $0 - \pi$ SQUID: all the lobes are similar in width, and I_c is suppressed around zero. By increasing the H_y to 40 mT, the vortex core has traveled over 100 nm away from the junction (Figure 4.4e). Interestingly, we find the

I_c to recover for zero out-of-plane field. This reentrant behavior is accompanied by drastic changes to the $I_c(B)$-pattern. The central lobe is now twice as wide, indicating a modified supercurrent distribution, which no longer corresponds to the original two channels. Even more striking is the amplitude of the I_c oscillations: instead of decaying, the lobes grow taller as we increase the magnitude of the out-of-plane field. This is the universal characteristic of $0 - \pi$ junctions, i.e., a junction consisting of multiple 0 and π segments connected in parallel[53–55]. Note that the observed evolution of the interference pattern with the in-plane field cannot be attributed to stray fields or misalignment with the magnet axes since the $I_c(B)$-patterns are independent of magnetic field sweep direction. More importantly, the behavior is completely absent in control samples with no LRT component (see Appendix A), which yield Fraunhofer-like patterns, regardless of the amplitude or direction of the in-plane field.

4.5. MODELING LRT GENERATION AT THE RIMS OF THE DISK

To analyze the generation of LRT correlations at the rim of the disk, we will use the linearised Usadel equations, which are spin-charge coupled diffusion equations for superconductors[7, 56]. They read:

$$[D\nabla^2 - 2(\omega + 3/\tau_{\text{sf}})]f_s + 2(\boldsymbol{h} \cdot \boldsymbol{f}) = 0 \tag{4.1}$$

$$[D\nabla^2 - 2(\omega + 1/\tau_{\text{sf}})]\boldsymbol{f} - 2f_s\boldsymbol{h} = 0 \tag{4.2}$$

where D is diffusion coefficient, $\boldsymbol{h}$ is the exchange field proportional to the magnetic moment, τ_{sf} is the spin relaxation rate and ω is the Matsubara frequency. $\hat{f}$ is the anomalous Green's function which takes into account triplet and singlet superconducting correlations, which is defined as:

$$\hat{f} = f_s\hat{\sigma}_0 + i(\boldsymbol{f} \cdot \hat{\boldsymbol{\sigma}}) \tag{4.3}$$

Here $\hat{\sigma}_0$ and $\hat{\boldsymbol{\sigma}}$ are the Pauli spin matrices, the first term corresponds to the singlet component, and the last three terms encode the triplet components. In the Supporting Information of the published material[57], we present the full technical details of the Usadel calculations; here, I present the main findings of said calculations. We now continue by describing the mechanism behind the formation of the rim currents using a model that links the vortex spin texture to the SOC.

4.5.1. MAPPING SPIN TEXTURE TO SPIN-ORBIT COUPLING

Within the cobalt weak link, the gradient of the local spin texture of the disk junctions is, at the rims of the device, not substantially larger than that of a bar-shaped device. This implies that, even though the LRT currents emerge at the rims, they are formed by a process that is sensitive to the global spin texture of the disk.
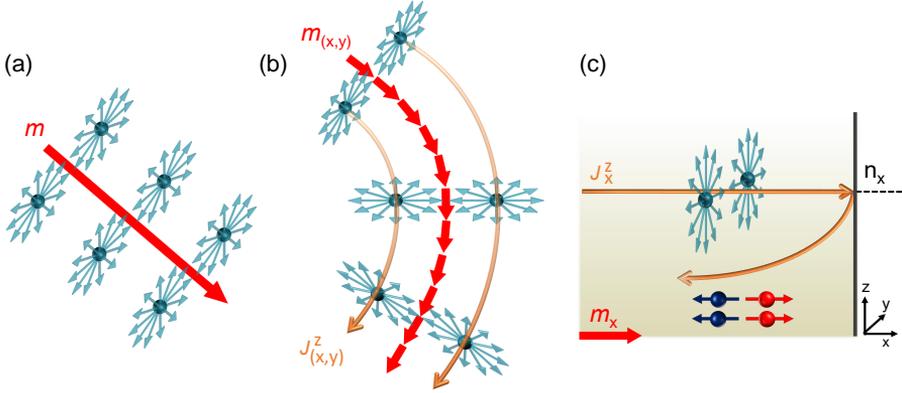

Figure 4.5: (a) SRT Cooper pairs (cyan) in a system with uniform magnetization. The SRT correlations have zero spin projection along the quantization axis, defined by the local magnetization vector $\boldsymbol{m}$ (red arrow). No equilibrium spin current (ESC) or LRT pairs are generated. (b) In the presence of spin texture, the SRT pairs continuously alter the orientation of their spin plane to remain normal to the local magnetization vector $\boldsymbol{m}_{(x,y)}$, producing an ESC $J^z_{(x,y)}$ (orange arrows), which adiabatically follows the local spin gauge field $\nabla\theta_v = (\boldsymbol{m} \times \nabla\boldsymbol{m})_z$. (c) When the ESC is incident on a bilayer−vacuum boundary, the adiabatic approximation breaks down. As the ESC cannot propagate outside the bilayer, the total spin current at the boundary must remain zero. To compensate for the adiabatic spin current, a condensate of LRT pairs (in red and blue) with $S_x = \pm1$ emerges near the vacuum boundary to generate an opposing spin current. Schematic courtesy of Kaveh Lahabi.

It was demonstrated that the combination of SOC and exchange field [35, 45, 47] or Zeeman field [44, 58] can result in an equilibrium spin current (ESC) which accumulates at the superconducting/vacuum boundaries. A similar process occurs in the presence of spin texture $\boldsymbol{m}(r)$, which produces the pure gauge SU(2) field that acts as effective spin-orbit coupling denoted by $i\hat{U}^\dagger\nabla\hat{U}$[33, 34, 59]. Here, $\hat{U}(\boldsymbol{r})$ is the spin-rotation matrix, determined by the transformation to the local spin quantization axis. Note that the vortex spin texture $\boldsymbol{m} = m(-\sin\theta_v, \cos\theta_v, 0)$ can be transformed into a uniform one by applying this spin-rotation operation. This induces an effective SOC term $i\hat{U}^\dagger\nabla\hat{U}\,\hat{\sigma}_z\nabla\theta_v$, through the spatial derivative of $\hat{f}$:

$$\nabla_j\hat{f} \rightarrow \nabla_j\hat{f} + i\nabla_j\theta_v[\hat{\sigma}_z, \hat{f}] = \hat{\boldsymbol{\sigma}}(\nabla_j\boldsymbol{f} - \nabla_j\theta_v[\boldsymbol{z} \times \boldsymbol{f}]) \tag{4.4}$$

Where $j = x, y, z$ is the index in coordinate space and $\theta_v = \arctan[(y - y_v)/(x - x_v)]$ (x_v, y_v are the coordinates of the vortex center). Hence, our system is analogous to one with an uniform magnetization and an intrinsic, spatially-inhomogeneous, SOC with the amplitude $|\nabla\theta_v| = 1/r_v$ (where r_v is the distance to the vortex core: $r_v = \sqrt{(x - x_v)^2 + (y - y_v)^2}$), and therefore hosts the aforementioned ESC.

The ESC is carried by the SRT Cooper pairs, which spontaneously appear both at the bottom of the S electrodes and at the top of the F layer. The ESC can be thought of as a spin-imbalance in this SRT condensate. The direction of the ESC is determined by the in-plane gradients of the magnetic texture and flows parallel to the S−F interface. In terms of $\boldsymbol{f}$ it then becomes $J_j^\gamma \propto |f_{SRT}|^2 (\boldsymbol{m} \times \nabla_j \boldsymbol{m})_\gamma$ (here $\gamma = x, y, z$ is the index in spin space). A ferromagnetic vortex texture yields $J_j^z \propto |f_{SRT}|^2 \nabla_j \theta_v = |f_{SRT}|^2 m_j / r_v$ which is in accordance with the general gauge-invariant expression for the spin current[60].

4.5.2. MECHANISM FOR GENERATING LRT RIM CURRENTS

Having established the equivalency between spin texture and SOC, we now provide a possible mechanism that relates the ESC to the emergence of LRT rim currents (see Figure 4.5 for a schematic representation). In the absence of spin texture, there is no ESC (Figure 4.5a). If the spin texture gradient is nonzero, the ESC adiabatically follows the local spin gauge field ($\boldsymbol{J}^z \parallel \nabla\theta_v = (\boldsymbol{m} \times \nabla\boldsymbol{m})_z$; see Figure 4.5b). When the spin current encounters the bilayer−vacuum boundary (for instance, due to deviations from the ideal circular geometry) the adiabatic approximation breaks down, resulting in an accumulation of spin at the rims of the device. Naturally, the spin accumulation decays over the spin diffusion length, which for cobalt is approximately 60 nm[61]. Near the interface, the adiabatic ESC can develop a non-zero normal component $\boldsymbol{m} \times (n_j \nabla_j)\boldsymbol{m} \neq 0$, where $\boldsymbol{n}$ is the interface normal. Since the total spin current is zero across the boundary, $n_j J_j^z = 0$, the ESC is compensated by a spin current carried by an LRT condensate, which emerges near the vacuum boundary (Figure 4.5c). This leads to a coupling between $\boldsymbol{f}_{SRT} \parallel \boldsymbol{m}$ and $\nabla\boldsymbol{f}_{LRT} \perp \boldsymbol{m}$, such that:

$$(\boldsymbol{n}\nabla)\boldsymbol{f} = -(n_j \nabla_j \theta_v)[\boldsymbol{z} \times \boldsymbol{f}] \tag{4.5}$$

Here the right-hand side of Eq. 4.5 contains the spin current perpendicular to the bilayer−vacuum boundary. A similar SRT to LRT conversion process has been proposed to occur at the sample boundaries of S−N−S junctions with intrinsic SOC and a spin active interface[46] or in one-dimensional systems with a geometric curvature[47].
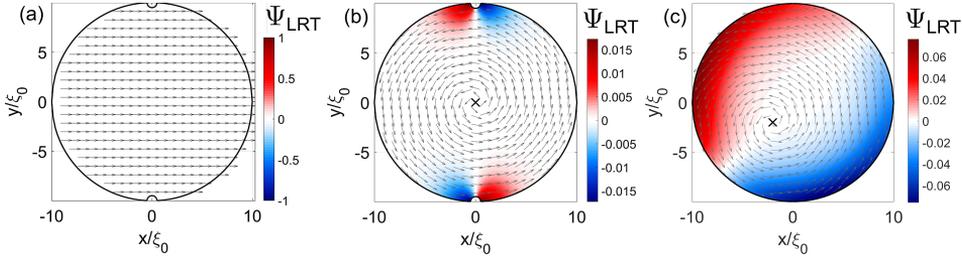
Figure 4.6: Simulated distribution of Ψ_{LRT} in a S/F bilayer for three different spin configurations, where the amplitude is normalized to $(\gamma\xi_0)f_{\text{SRT}}$ (γ is the S−F interface transparency). Arrows show the direction of the in-plane spin texture. The simulated geometry includes notches that arise from FIB processing of the actual devices. (a) A homogeneous magnetization, where LRT correlations are completely absent. (b) In the presence of a magnetic vortex, LRT Cooper pairs are generated at the notches, forming two LRT current channels. (c) If the vortex core is shifted from the junction, an asymmetry arises between the signs of the LRT channels, resulting in $0-\pi$ SQUID-like configuration, also in the absence of the notches. Image courtesy of Mikhail Silaev.

By solving the linearized Usadel equation for a 2D disk-shaped S−F bilayer (without the trench), we simulate the distribution of the LRT amplitude Ψ_{LRT}, where $\boldsymbol{f}_{\text{LRT}} = \Psi_{\text{LRT}}(m_y, -m_x, 0)$. The results for three different spin textures are presented in Figure 4.6. For a uniform magnetization, the LRT correlations are completely absent, regardless of sample geometry (Figure 4.6a). For a perfectly symmetric vortex pattern, any deviation from the ideal circular geometry at the sample−vacuum boundary (i.e., rim roughness or disorder) results in the emergence of LRT correlations. In our simulation (Figure 4.6a,b), we use notches on the sides of the disk, also present in our devices, to demonstrate the effect of nonideal boundaries. However, in practice, any deviation from the perfect circular geometry or disorder at boundaries results in a similar outcome. Interestingly, even in the ideal circular geometry with flawless boundaries (i.e., atomically clean and smooth edges), the LRT currents would still appear if the magnetic vortex is not perfectly centered (see Figure 4.6c). Note that for perfect circular symmetry, with the vortex at the center, J_j^z will always remain parallel to m_j and no LRT is generated.

Our simulations also provide insights into the phase of LRT correlations. When the vortex core is aligned with the trench (at $x = 0$), the LRT currents will result in two π-channels, as indicated by the sign change of Ψ_{LRT}. In Figure 4.6c, the vortex is displaced from the center (e.g., due to an in-plane field), and the LRT channels develop opposite signs at the trench. This asymmetry is consistent with the observed $0-\pi$ SQUID interference pattern, measured under a constant in-plane field (Figure 4.4).

4.6. DISCUSSION

While the model presented here can describe the emergence of LRT correlations at the bilayer−vacuum boundaries and the appearance of spontaneous supercurrents in our

junctions (i.e., $0 - \pi$ segments), we should point out that this formalism is restricted to 2D slices of the bilayer. Accounting for the superconductor-vacuum interface formed by the trench is more challenging, as it requires a full three-dimensional model and the knowledge of the exact trench dimensions (e.g., its extent in the Co layer).[2]

It should be noted that there is a fundamental difference between the devices presented here and those reported in a previous work, where the disk-shaped junctions consisted of a magnetic multilayer ($S-F'-F-F''-S$)[21]. In contrast to the Nb/Ni/Cu/Co/Cu/Ni/Nb junctions, where long-range proximity was the result of the magnetic noncollinearity between the Co and Ni layers, the LRT correlations of the devices presented here, are generated directly by the spin texture of a single ferromagnet. This is evident from the irreversible enhancement of I_c by magnetic conditioning of the Ni 1.5 nm layer. In contrast, in the case of single ferromagnet devices, the transport characteristics are unaltered by magnetic conditioning. The vortex magnetization is the global ground state of the Co-disk: regardless of the magnetic history, the disk will revert to the vortex magnetization at zero field, which is confirmed by micromagnetic simulations. Furthermore, both types of devices exhibit radically different behavior as a function of in-plane fields. However, there are similarities: both devices show a two-channel interference pattern, although the current channels are considerably more confined in the case of a single ferromagnetic weak link.

4.7. CONCLUSION

In summary, we have revealed the interplay between triplet superconductivity and magnetic texture, which manifests as LRT supercurrents localized at the rim of the ferromagnet. We elucidate the origin of the rim currents by mapping the magnetic texture to an effective SOC, which leads to the emergence of equilibrium spin currents – carried by the triplet Cooper pairs present at the $S-F$ interface. We also propose a mechanism for converting the spin currents into equal-spin LRT correlations based on the breakdown of the adiabatic approximation at the sample−vacuum boundaries. Lastly, we show that the nature of LRT transport undergoes drastic changes when the spin texture is modified. As illustrated here, by applying relatively small magnetic fields, the same Josephson junction can be tuned to function as both standard (0-0) and $0 - \pi$ SQUIDs. The capacity to control supercurrents with the spin texture of a single ferromagnetic layer opens exciting prospects for regulating transport in superconducting devices. Since the curie temperature of the ferromagnet far exceeds the superconducting critical temperature, these spin-textured SF-hybrid devices form a prime candidate for researching non-volatile superconducting memory elements, which is the topic of the following chapter.

---

[2]For a further discussion on this topic, the reader is referred to the supplementary information of reference [57].

APPENDICES

A. CONTROL EXPERIMENTS

In this Appendix, we establish the vital role of spin texture in generating long-range triplet (LRT) correlations. Furthermore, we show that junctions, where singlet correlations dominate transport, are not affected by the spin texture and that the two-channel behavior is absent.

We fabricated control samples with a rectangular configuration, where the Co layer is uniformly magnetized along its long axis (i.e., having no spin texture). The bar-shaped devices have equal width (1 µm) and layer thicknesses as the triplet disk devices (see top inset of Figure A.1a). Due to the 5:1 aspect ratio, no magnetic vortex is stable in the cobalt layer. The same focused ion beam milling procedure was applied to form the weak link. Figure A.1a shows the resistance versus temperature of five of such junctions. For devices A to D a similar Ga-ion dose is used for preparing the trench as the triplet disk devices (Nb is completely removed from the weak link). In device E, however, the weak link is fabricated by applying a lower dose, which results in the incomplete removal of the Nb layer in the trench. As shown in Figure A.1a, only device E shows signs of short-range proximity effect, with a heavily suppressed critical current. Figure A.1b shows the $I_c(B)$-pattern of device E. In contrast to the triplet disk junctions, we observe a distorted single-channel pattern with a rapidly decaying $I_c(B)$. The pattern is shifted and distorted due to the magnetic dipole fields of the ferromagnet.
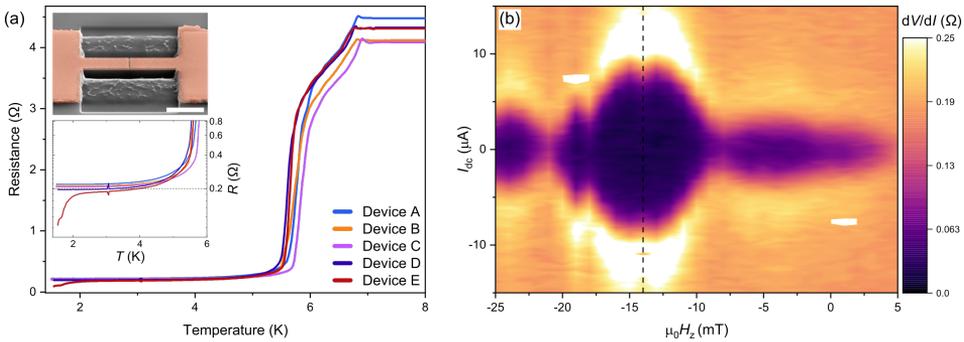

Figure A.1: (a) Resistance versus temperature obtained on five bar-shaped junctions lacking any spin texture, using a measurement current of 10 µA. The weak link in devices A to D is fabricated following the same method as the triplet disk devices. The low T resistance of these devices equals the weak link resistance (0.2 Ω). As seen from the lower inset, only device E shows weak signs of proximity effect, with a heavily suppressed critical current. This device was fabricated using a lower Ga-ion dose, resulting in an Nb-residue in the weak link. The top inset shows a false-colored scanning electron micrograph of a bar junction where the scale bar corresponds to 2 µm. (b) shows the $I_c(B)$-pattern obtained on device E. The Fraunhofer-like pattern indicates a uniform current distribution throughout the weak link. The middle lobe is shifted to -14 mT due to the magnetic stray fields of the ferromagnet.
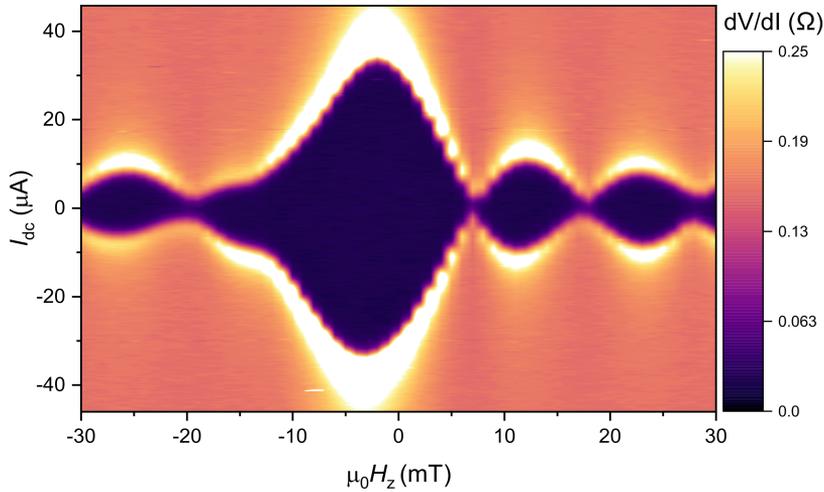
Figure A.2: $I_c(B)$-pattern recorded on a disk-shaped sample containing a shallow trench (i.e., with a Nb-residue in the weak link) and therefore dominated by singlet transport. The central peak is twice as wide as neighboring ones, and the peak height decreases in a $1/B$ fashion. Superconductivity in this sample is found to be unaffected by the removal of the spin texture of the ferromagnet by the application of an in-plane field.

Additionally, we fabricated disk-shaped control samples where the Nb is not completely removed from the weak link to study the interaction of singlet supercurrents with the vortex spin texture. Figure A.2 shows an $I_c(B)$-pattern of such a device. Contrary to the triplet devices, we observe a clear single-channel Fraunhofer-like pattern with the central lobe being twice as wide as the subsequent ones and a $1/B$ decay of the peak height. The missing minimum on the negative field side of the pattern may be attributed to a nearby Abrikosov vortex in one of the superconducting leads[62]. This demonstrates that, despite the ferromagnetic vortex in the Co-layer, the singlet supercurrent is distributed uniformly across the junction. Note that conventional weak link devices maintain their critical current, even when the spin texture is removed by applying an in-plane field. In Figure A.3 we compare the behavior of a device with triplet channels to that of a device with a shallow trench, i.e., a conventional weak link, under the influence of an in-plane field H_y along the trench. The triplet device shows variations in I_c due to 0-π transitions and vice versa, and the disappearance of the critical current around 180 mT. The conventional device containing the shallow trench (Figure A.2) retains an I_c of around 10 μA up to 2 T.

Finally, it must be noted that the two-channel behavior is not a trivial consequence of the disk configuration or a byproduct of the FIB milling used in forming the weak link, as is demonstrated by the interference patterns obtained on the S−N−S junctions presented in Chapter 3. For all those devices, we found an undistorted single-channel $I_c(B)$-pattern, corresponding to a uniform distribution of supercurrent in the junction. To summarize, our control experiments demonstrate that the rim channels only ap-
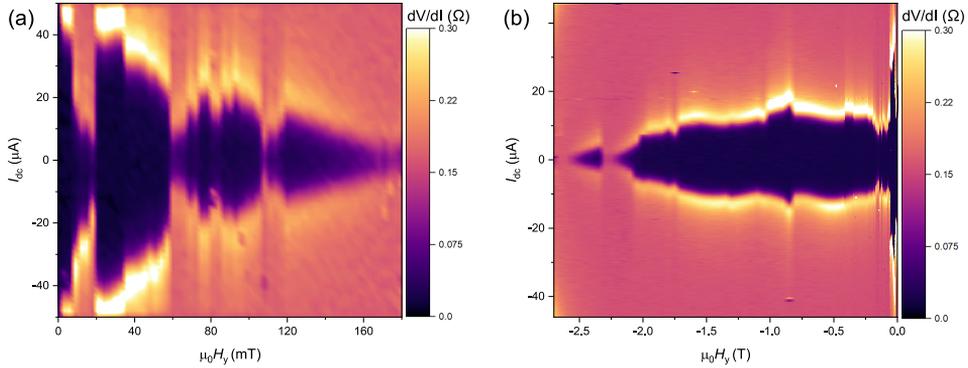
Figure A.3: In-plane $I_c(H_y)$ for a sample with triplet channels and a sample with a conventional weak link. (a) The triplet sample loses its critical current above 180 mT in-plane field along the trench. At these fields, the spin texture of the disk has become uniform and therefore the generator for LRT correlations is absent. On the sample in (a) we obtained the data shown in Figure 4.4. (b) The sample with a shallow trench retains a I_c up to above 2 T, far above the fields required for stabilizing a uniform spin texture.

pear when transport is carried by the LRT correlations. In contrast to singlet or SRT transport, the LRT currents are also highly sensitive to the changes in cobalt spin texture, which are brought about by relatively small in-plane fields.

REFERENCES

[1] Sato, M. & Ando, Y. Topological superconductors: a review. *Rep. Prog. Phys.* **80**, 076501 (2017).

[2] Hart, S. *et al.* Induced superconductivity in the quantum spin Hall edge. *Nat. Phys.* **10**, 638–643 (2014).

[3] Murani, A. *et al.* Ballistic edge states in Bismuth nanowires revealed by SQUID interferometry. *Nat. Commun.* **8**, 15941 (2017).

[4] Allen, M. T. *et al.* Spatially resolved edge currents and guided-wave electronic states in graphene. *Nat. Phys.* **12**, 128–133 (2016).

[5] Robinson, J. W. A., Piano, S., Burnell, G., Bell, C. & Blamire, M. G. Critical Current Oscillations in Strong Ferromagnetic π Junctions. *Phys. Rev. Lett.* **97**, 177003 (2006).

[6] Bergeret, F. S., Volkov, A. F. & Efetov, K. B. Long-range proximity effects in superconductor-ferromagnet structures. *Phys. Rev. Lett.* **86**, 4096 (2001).

[7] Bergeret, F. S., Volkov, A. F. & Efetov, K. B. Odd triplet superconductivity and related phenomena in superconductor-ferromagnet structures. *Rev. Mod. Phys.* **77**, 1321 (2005).

[8] Eschrig, M. & Löfwander, T. Triplet supercurrents in clean and disordered half-metallic ferromagnets. *Nat. Phys.* **4**, 138–143 (2008).

[9] Keizer, R. S. *et al.* A spin triplet supercurrent through the half-metallic ferromagnet CrO_2. *Nature* **439**, 825–827 (2006).

[10] Anwar, M. S., Czeschka, F., Hesselberth, M., Porcu, M. & Aarts, J. Long-range supercurrents through half-metallic ferromagnetic CrO_2. *Phys. Rev. B* **82**, 100501 (2010).

[11] Singh, A., Jansen, C., Lahabi, K. & Aarts, J. High-Quality CrO_2 Nanowires for Dissipation-less Spintronics. *Phys. Rev. X* **6**, 041012 (2016).

[12] Linder, J. & Robinson, J. W. A. Superconducting spintronics. *Nat Phys* **11**, 307–315 (2015).

[13] Eschrig, M. Spin-polarized supercurrents for spintronics: a review of current progress. *Rep. Prog. Phys.* **78**, 104501 (2015).

[14] Houzet, M. & Buzdin, A. I. Long range triplet Josephson effect through a ferromagnetic trilayer. *Phys. Rev. B* **76**, 060504 (2007).

[15] Khaire, T. S., Khasawneh, M. A., Pratt, W. P. & Birge, N. O. Observation of spin-triplet superconductivity in Co-based Josephson junctions. *Phys. Rev. Lett.* **104**, 137002 (2010).

[16] Robinson, J. W. A., Witt, J. D. S. & Blamire, M. G. Controlled injection of spin-triplet supercurrents into a strong ferromagnet. *Science* **329**, 59 (2010).

[17] Anwar, M. S., Veldhorst, M., Brinkman, A. & Aarts, J. Long range supercurrents in ferromagnetic CrO_2 using a multilayer contact structure. *Appl. Phys. Lett.* **100**, 052602 (2012).

[18] Leksin, P. V. *et al.* Evidence for triplet superconductivity in a superconductor-ferromagnet spin valve. *Phys. Rev. Lett.* **109**, 1–5 (2012).

[19] Iovan, A., Golod, T. & Krasnov, V. M. Controllable generation of a spin-triplet supercurrent in a Josephson spin valve. *Phys. Rev. B* **90**, 134514 (2014).

[20] Martinez, W. M., Pratt, W. P. & Birge, N. O. Amplitude Control of the Spin-Triplet Supercurrent in S/F/S Josephson Junctions. *Phys. Rev. Lett.* **116**, 1–5 (2016).

[21] Lahabi, K. *et al.* Controlling supercurrents and their spatial distribution in ferromagnets. *Nat. Commun.* **8**, 2056 (2017).

[22] Kapran, O. M., Iovan, A., Golod, T. & Krasnov, V. M. Observation of the dominant spin-triplet supercurrent in Josephson spin valves with strong Ni ferromagnets. *Phys. Rev. Res.* **2**, 1–10 (2020).

[23] Aguilar, V. *et al.* Spin-polarized triplet supercurrent in Josephson junctions with perpendicular ferromagnetic layers. *Phys. Rev. B* **102**, 024518 (2020).

[24] Komori, S. *et al.* Spin-orbit coupling suppression and singlet-state blocking of spin-triplet Cooper pairs. *Sci. Adv.* **7**, eabe0128 (2021).

[25] Fominov, Y. V., Volkov, A. F. & Efetov, K. B. Josephson effect due to the long-range odd-frequency triplet superconductivity in SFS junctions with Néel domain walls. *Phys. Rev. B* **75**, 104509 (2007).

[26] Volkov, A. F. & Efetov, K. B. Odd triplet superconductivity in a superconductor/ferromagnet structure with a narrow domain wall. *Phys. Rev. B* **78**, 1–11 (2008).

[27] Kalcheim, Y., Kirzhner, T., Koren, G. & Millo, O. Long-range proximity effect in $La_{2/3}Ca_{1/3}MnO_3$/(100)$YBa_2Cu_3O_{7-\delta}$ ferromagnet/superconductor bilayers: Evidence for induced triplet superconductivity in the ferromagnet. *Phys. Rev. B* **83**, 2–7 (2011).

[28] Aikebaier, F., Virtanen, P. & Heikkilä, T. Superconductivity near a magnetic domain wall. *Phys. Rev. B* **99**, 1–11 (2019).

[29] Silaev, M. A. Possibility of a long-range proximity effect in a ferromagnetic nanoparticle. *Phys. Rev. B* **79**, 184505 (2009).

[30] Kalenkov, M. S., Zaikin, A. D. & Petrashov, V. T. Triplet superconductivity in a ferromagnetic vortex. *Phys. Rev. Lett.* **107**, 087003 (2011).

[31] Bhatia, E. *et al.* Nanoscale Domain Wall Engineered Spin-Triplet Josephson Junctions and SQUID. *Nano Lett.* **21**, 3092–3097 (2021).

[32] Niu, Z. A spin triplet supercurrent in half metal ferromagnet/superconductor junctions with the interfacial rashba spin-orbit coupling. *Appl. Phys. Lett.* **101**, 062601 (2012).

[33] Bergeret, F. S. & Tokatly, I. V. Singlet-triplet conversion and the long-range proximity effect in superconductor-ferromagnet structures with generic spin dependent fields. *Phys. Rev. Lett.* **110**, 117003 (2013).

[34] Bergeret, F. S. & Tokatly, I. V. Spin-orbit coupling as a source of long-range triplet proximity effect in superconductor-ferromagnet hybrid structures. *Phys. Rev. B* **89**, 134517 (2014).

[35] Alidoust, M. & Halterman, K. Spontaneous edge accumulation of spin currents in finite-size two-dimensional diffusive spin–orbit coupled SFS heterostructures. *New J. Phys.* **17**, 033001 (2015).

4

[36] Jacobsen, S. H., Ouassou, J. A. & Linder, J. Critical temperature and tunneling spectroscopy of superconductor-ferromagnet hybrids with intrinsic rashba-dresselhaus spin-orbit coupling. *Phys. Rev. B* **92**, 024510 (2015).

[37] Satchell, N. & Birge, N. O. Supercurrent in ferromagnetic Josephson junctions with heavy metal interlayers. *Phys. Rev. B* **97**, 1–8 (2018).

[38] Jeon, K. R. *et al.* Enhanced spin pumping into superconductors provides evidence for superconducting pure spin currents. *Nat. Mater.* **17**, 499–503 (2018).

[39] Bujnowski, B., Biele, R. & Bergeret, F. S. Switchable Josephson current in junctions with spin-orbit coupling. *Phys. Rev. B* **100**, 1–9 (2019).

[40] Eskilt, J. R., Amundsen, M., Banerjee, N. & Linder, J. Long-ranged triplet supercurrent in a single in-plane ferromagnet with spin-orbit coupled contacts to superconductors. *Phys. Rev. B* **100**, 224519 (2019).

[41] Jeon, K. R. *et al.* Tunable Pure Spin Supercurrents and the Demonstration of Their Gateability in a Spin-Wave Device. *Phys. Rev. X* **10**, 31020 (2020).

[42] Satchell, N., Loloee, R. & Birge, N. O. Supercurrent in ferromagnetic Josephson junctions with heavy-metal interlayers. II. Canted magnetization. *Phys. Rev. B* **99**, 174519 (2019).

[43] Silaev, M. A., Bobkova, I. V. & Bobkov, A. M. Odd triplet superconductivity induced by a moving condensate. *Phys. Rev. B* **102**, 100507 (2020).

[44] Tokatly, I. V., Bujnowski, B. & Bergeret, F. S. Universal correspondence between edge spin accumulation and equilibrium spin currents in nanowires with spin-orbit coupling. *Phys. Rev. B* **100**, 214422 (2019).

[45] Bobkova, I. V. & Barash, Y. S. Effects of spin-orbit interaction on superconductor-ferromagnet heterostructures: Spontaneous electric and spin surface currents. *J. Exp. Theor.* **80**, 494–499 (2004).

[46] Alidoust, M. & Halterman, K. Long-range spin-triplet correlations and edge spin currents in diffusive spin–orbit coupled SNS hybrids with a single spin-active interface. *J. Condens. Matter Phys.* **27**, 235301 (2015).

[47] Salamone, T., Svendsen, M. B. M., Amundsen, M. & Jacobsen, S. Curvature-induced long ranged supercurrents in diffusive SFS Josephson Junctions, with dynamic $0 - \pi$ transition. *Phys. Rev. B* **104**, L060505 (2021).

[48] Mazanik, A. A. & Bobkova, I. V. Supercurrent-induced long-range triplet correlations and controllable Josephson effect in superconductor/ferromagnet hybrids with extrinsic spin-orbit coupling. *Phys. Rev. B* **105**, 144502 (2022).

[49] Bobkova, I. V., Bobkov, A. M. & Silaev, M. A. Dynamic spin-triplet order induced by alternating electric fields in superconductor-ferromagnet-superconductor Josephson junctions. *Phys. Rev. Lett.* **127**, 147701 (2021).

[50] Prejbeanu, I. L. *et al.* In-plane reversal mechanisms in circular Co dots. *J. Appl. Phys.* **91**, 7343–7345 (2002).

[51] Natali, M. *et al.* Correlated magnetic vortex chains in mesoscopic cobalt dot arrays. *Phys. Rev. Lett.* **88**, 157203 (2002).

[52] Glick, J. A. *et al.* Phase control in a spin-triplet SQUID. *Sci. Adv.* **4**, 1–8 (2018).

[53] Smilde, H. J. H. *et al.* d-Wave–Induced Josephson current counterflow in YBa$_2$Cu$_3$O$_7$/Nb zigzag junctions. *Phys. Rev. Lett.* **88**, 057004 (2002).

[54] Scharinger, S. *et al.* Interference patterns of multifacet $20 \times (0-\pi)$ Josephson junctions with ferromagnetic barrier. *Phys. Rev. B* **81**, 174535 (2010).

[55] Gürlich, C. *et al.* Visualizing supercurrents in ferromagnetic Josephson junctions with various arrangements of 0 and π segments. *Phys. Rev. B* **81**, 094502 (2010).

[56] Usadel, K. D. Generalized diffusion equation for superconducting alloys. *Phys. Rev. Lett.* **25**, 507–509 (1970).

[57] Fermin, R. *et al.* Superconducting triplet rim currents in a spin-textured ferromagnetic disk. *Nano Letters* **22**, 2209–2216 (2022).

[58] Bergeret, F. S. & Tokatly, I. V. Theory of the magnetic response in finite two-dimensional superconductors. *Phys. Rev. B* **102**, 060506(R) (2020).

[59] Tokatly, I. Equilibrium spin currents: non-abelian gauge invariance and color diamagnetism in condensed matter. *Phys. Rev. Lett.* **101**, 106601 (2008).

[60] Hill, D., Slastikov, V. & Tchernyshyov, O. Chiral magnetism: a geometric perspective. *SciPost Phys.* **10**, 78 (2021).

[61] Bass, J. & Pratt, W. P. Spin-diffusion lengths in metals and alloys, and spin-flipping at metal/metal interfaces: an experimentalist's critical review. *J. Condens. Matter Phys.* **19**, 183201 (2007).

[62] Golod, T., Pagliero, A. & Krasnov, V. M. Two mechanisms of Josephson phase shift generation by an Abrikosov vortex. *Phys. Rev. B* **100**, 174511 (2019).

4